High-throughput experimentation unveils composition – Structure – Conductivity relationships in the extended LiPON system

William Berthou, Maxime Legallais, Stéphanie Sorieul, Gunay Yildirim, Bruno Bousquet, Vincent Motto-Ros, Frédéric Le Cras

ADVANCED ENERGY MATERIALS
www.advenergymat.de

High-Throughput Experimentation Unveils Composition – Structure – Conductivity Relationships in the Extended LiPON System

*William Berthou, Maxime Legallais, Stéphanie Sorieul, Gunay Yildirim, Bruno Bousquet, Vincent Motto-Ros, and Frédéric Le Cras**

A high-throughput experimental approach is developed to assess the correlations between chemical composition, structure and conduction properties of inorganic solid ionic conductors. This approach covers the preparation of a large number of samples by combinatorial synthesis, followed by fast characterization of the material library. The approach is primarily based on combinatorial synthesis by magnetron co-sputtering and the characterization of thin film samples where lithium phosphorus oxynitride (LiPON) is chosen as a case study. A library of 76 LiPON materials is prepared in one experiment from the reactive co-sputtering of LiPO3 and Li3PO4 in a N2 atmosphere. A specific sample design allows conducting thickness and impedance measurements, Raman spectroscopy, then fast and spatially-resolved chemical analysis by Laser-Induced Breakdown Spectroscopy (LIBS) on each material. Particular developments are devoted to this technique to achieve quantitative analysis of lithium in thin films. The materials cover a wide range of compositions with 0.95<Li/P<2.03 and a high N/P nitrogen content of ≈1.0-1.2.
Two distinct compositional ranges can be distinguished. For 0.95<Li/P<1.2, conductivity increases and the PO3− chains gradually disappear, whereas for 1.2<Li/P<2.03, conductivity stabilizes despite continuous structural evolution, in parallel with an increase in charge carrier concentration.

1. Introduction

Amorphous solid Li^+ ion conductors have been investigated for decades for their possible applications in all-solid-state sensors, electrochromic systems, or lithium batteries. These materials can be prepared under the form of bulk glasses by melt-quenching or as thin films by physical vapour deposition.[1–4] They are composed of at least one glass former, such as B,[5,6] Si,[7–11] Ge, P,[12,13] W, lithium as a glass modifier, and mainly oxygen or sulphur as anions.[14] One noticeable advantage of these amorphous or glassy compounds is that their composition can be changed over a wide range. Their amorphous character results from a random arrangement of tetrahedral or trigonal planar units sharing a common (bridging) anion, which constitutes the structural network. The presence of Li modifies the structure of the network by reducing the number of

W. Berthou, M. Legallais, G. Yildirim
CEA
CEA Tech Nouvelle Aquitaine
Pessac F-33600, France
W. Berthou, B. Bousquet, F. Le Cras
CNRS
Bordeaux INP
Institut de Chimie de la Matière Condensée de Bordeaux
ICMCB, UMR 5026
Univ. Bordeaux
Pessac F-33600, France
E-mail: frederic.lecras@cea.fr

The ORCID identification number(s) for the author(s) of this article can be found under https://doi.org/10.1002/aenm.202400656

DOI: 10.1002/aenm.202400656

S. Sorieul
LP2iB
UMR 5797
Université de Bordeaux
CNRS
Gradignan F-33170, France
V. Motto-Ros
Institut Lumière Matière
Univ. Lyon
Université Claude Bernard Lyon 1
CNRS
UMR 5306
Villeurbanne F-69100, France
F. Le Cras
CEA
LITEN
Univ. Grenoble Alpes
Grenoble F-38000, France

covalent bonds and generating non-bridging anions carrying a negative charge near Li^+ ions. When the concentration of Li^+ is sufficiently high, the induced structural changes in the network and the large concentration of charge carriers allow long-range transport of ionic species in the material. Composition, in terms of both stoichiometry and the chemical nature of the components, is the main parameter influencing the structure of these amorphous materials on a local scale and consequently their functional properties, starting with ionic conductivity. Levers for improving the ionic conductivity and reducing the activation energy are for example (i) the introduction of a second glass former that profoundly modifies the energy landscape for ion migration, giving rise to the so-called Mixed Glass Former Effect (MGFE), (ii) anionic substitutions that modify the binding energy between Li^+ and the network or the free volume around Li^+ sites, (iii) adjustment of the concentration of mobile charge carriers. Considering this, it is understandable that the search for materials with, for example, maximum ionic conductivity, is likely to involve the pursuit of synergies between these different phenomena, and consequently the study of systems with compositions that are becoming very complex.

In this respect, the development of lithium phosphate based amorphous ion conductors is highly prominent. This system has been studied initially focusing on bulk glasses with compositions around $LiPO_3$, since the glass formation region of xLi_2O-$(1\text{-}x)P_2O_5$ corresponds approximately to $x < 0.4$. It was found that glassy $LiPO_3$ has a low ionic conductivity of about 2.10^{-9} $S.cm^{-1}$ at 298 K, and that the latter can be enhanced by two orders of magnitude by increasing x.[15] At the same time, nitridation of $LiPO_3$ melts was achieved for other purposes,[16,17] leading to a typical glass composition of $LiPO_{2.15}N_{0.57}$. Further investigation was conducted into the ionic conduction properties of these materials. The results demonstrated that the incorporation of N has a beneficial, albeit limited, effect on them.[18] Simultaneous substitution of oxygen by N and S was also assessed resulting in a moderate improvement in conductivity up to 3.10^{-7} $S.cm^{-1}$ for the $Li_{1.62}PO_{2.84}S_{0.11}N_{0.32}$ material.[19] Beneficial effects of a mixed glass former and a higher Li content on the Li^+ transport was evidenced in the Li_2O-B_2O_3-P_2O_5 system, but exploration of richer Li compositions was facing crystallization.[20] In the Li_2O-SiO_2-P_2O_5-LiCl system, the addition of Li halide and silica allowed to obtain glassy materials having a Li/P ratio slightly higher than 2.[21] Similar paths have been followed in the development of amorphous thin film electrolytes synthesized by magnetron sputtering, which offers the advantage of enabling the production of amorphous materials within a broader range of composition. Indeed, this synthesis method includes a step that can be considered as a hyper-quenching of elementary constituents deposited on a substrate at room temperature. The synthesis of thin films from a Li_3PO_4 target was an important step in these developments, demonstrating not only the possibility of obtaining Li-rich amorphous films, but also the incorporation of nitrogen by reactive sputtering under N_2.[22] By further tuning the target composition and sputtering conditions, Li/P and N/P ratios of up to 4.9 and 1.4 respectively were achieved.[23,24] Finally, the ionic conductivity of LiPON thin film materials is now more than ten times higher than that of bulk LiPON glasses. Further improvements exploiting the mixed glass former effect have been also sought in oxynitride thin films, in particular through the series of LiBPON and LiSiPON materials.[5,25,26] As a result, another performance milestone was achieved with the composition $Li_{1.35}Si_{0.79}P_{0.21}O_{1.98}N_{0.98}$, which exhibits a conductivity of 2.10^{-5} $S.cm^{-1}$ at RT and an activation energy of 0.47 eV.

This brief history and the studies mentioned above allow us to highlight in particular that (i) the application of multiple design rules in the search for optimum performance ultimately leads to complex materials where the separate effects of these rules becomes difficult to understand and predict (ii) the increasing complexity of materials' elemental compositions means that the study of new systems can only be carried out on specific, restricted compositional domains, or on broader domains that inevitably leave large ranges unexplored (iii) due to differences in synthesis methods, parameters or characterisation techniques, comparing and assembling separate studies within a compositional system can be challenging and potentially hinder a clear understanding of the relationships between composition, structure, and functional properties.

Implementing a High Throughput Experimental (HTE) approach could greatly help address these points. Such approach, first used in pharmaceuticals and now becoming more common in material science, aims at speeding up the discovery of new compounds and identifying the best performing materials for specific functional properties. It is also a powerful tool for documenting relationships between different material properties. This method combines the preparation of a large number of samples with varying compositions (i.e., material libraries) by combinatorial synthesis with the fast, automated physical-chemical characterization of these libraries by selected techniques. Different methods can be used for combinatorial synthesis including automated solid-state synthesis,[27] electrodeposition,[28] gel polymer diffusion and multiplume-pulsed laser deposition.[29,30] Magnetron sputtering (MS) is also widely used to prepare material libraries, particularly for studying metallic systems, but also ceramics. It can be carried out using different methods, based either on a sequential or simultaneous sputtering of several targets, generating compositional matrices or gradients onto a substrate.[31–33] It should be noted that magnetron sputtering was the synthesis method chosen by Dahn's group for studying Si-based anode materials in what was likely the first HTE work in the field of battery materials.[31]

In this work, we report on the development of a HTE workflow suitable for assessing amorphous thin film ion conductors, with a focus on lithium solid electrolytes. The LiPO(N) system is used as a first case study, with ionic conductivity as the probed functional property. As previously mentioned, this system has been thoroughly studied either under the form of bulk glasses (in the low Li/P and N/P region) or thin films (in the high Li/P and N/P region), therefore leaving some compositional domains unexplored. More importantly, these thin film materials are currently used in all-solid-state microbatteries and microsupercapacitors,[34–36] due to a combination of interesting properties: an ionic conductivity reaching $\sigma_{Li+} \sim 3.10^{-6}$ $S.cm^{-1}$ at 298K,[37] an electrochemical quasi-stability over a wide potential range (~[4-0] V versus Li^+/Li^0),[38] a high dielectric constant ($\epsilon \sim 14$) and very low electronic conductivity ($\sigma_{e^-} < 10^{-12}$ $S.cm^{-1}$).[36] LiPON thin films can also be used as coatings interposed between the electrolyte and the active material to prevent detrimental phenomena at the interface, in particular in all-solid-state batteries in

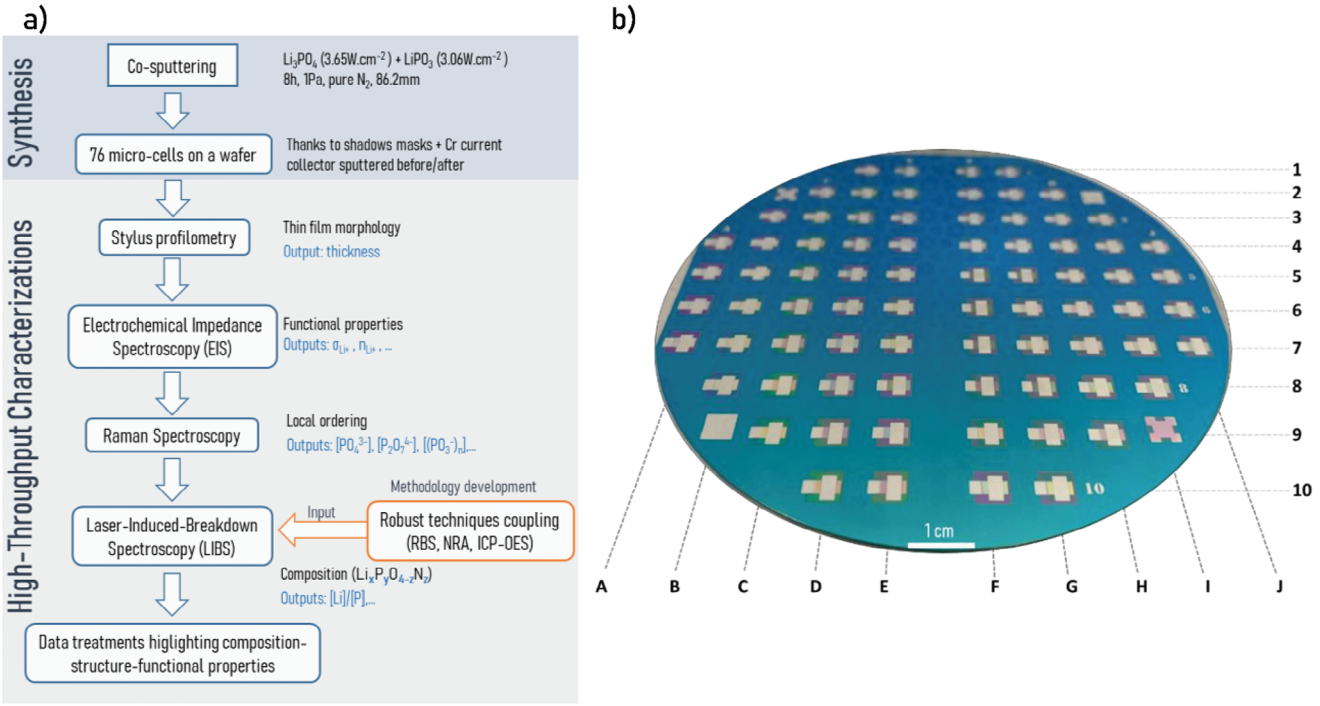

Figure 1. a) the HTE approach based on combinatorial synthesis by co-sputtering and a fast characterization workflow, b) the 76 sample library synthesized at once on a 4'' substrate and the sample identification system.

which they can hinder the propagation of lithium dendrites and inhibit the decomposition of the solid electrolyte.[26,39]

Herein, the method used to screen a wide range of compositions in the LiPON system is based on the combinatorial synthesis of thin film materials by reactive co-sputtering of multiple targets, followed by a sequence of dimensional, chemical, structural and electrical characterizations. The most challenging part of the process was rapid chemical mapping of thin-film material libraries, which required specific development to enable quantitative analysis of Li content.

2. Experimental Section

2.1. HTE Workflow

The full high throughput experimental workflow developed in this work is displayed in **Figure 1a**. As mentioned previously, it starts with the deposition of a thin film on a large substrate by magnetron co-sputtering that allows the spread of a composition gradient at the surface. This continuum of compositions is discretized into 76 individual samples using a shadow mask during deposition. Actually, the deposition of the LiPON film takes places between the deposition of two metal layers through two additional shadow masks. This patterned stack generates "micro-cells" (Figure 1b) that allow further electrical characterization of the samples.

The 76-sample library is then scanned using a series of appropriate characterisation techniques aimed at obtaining a first set of correlations between the composition, the structure and the ionic conductivity of LiPON materials. For the moment, these techniques comprise stylus profilometry to measure the sample's thickness, impedance spectroscopy to obtain the ionic conductivity amongst other electrical properties, Raman spectroscopy to highlight structural features at the local scale and newly introduced Laser-Induced Breakdown Spectroscopy (LIBS) for the chemical analysis.

Determination of the chemical composition appears to be the most challenging part of the workflow when it comes to analysing thin film lithium battery materials, since it requires a technique that combines (i) the ability to quantitatively analyse lithium (and possibly other light elements), (ii) a high sensitivity as the analyte amount is very limited (~µg), (iii) the ability to perform spatially resolved sampling & analysis (<1 mm^2), even on large specimens, and finally (iv) speed. Energy Dispersive X-ray analysis (EDX) or X-ray fluorescence which are the techniques commonly used to map libraries based on metallic materials are not applicable in this case since they lack one or more of the above requirements. The combination of Rutherford Backscattering Spectrometry (RBS), Deuteron-Induced Gamma-ray Emission and EDX, as implemented by *Borhani-Haghighi* et al. for the analysis of Li-Co-Mn-O thin films, can provide quantitative results, but is definitely not well suited to an HTE process.[40] The LIBS technique can offer a comprehensive solution to these challenging requirements.[41] This technique is based on the interaction of pulsed and focused laser beam with the surface of the sample. This interaction induces ablation, and vaporization of the matter and the formation of a plasma containing the chemical elements originating from the ablation crater. Radiations produced by the de-excitation processes, which are the signature of the chemical species present in the plasma, are measured by optical spectroscopy. The technique allows a fast multi-elemental analysis of small sample volume, including the lightest elements

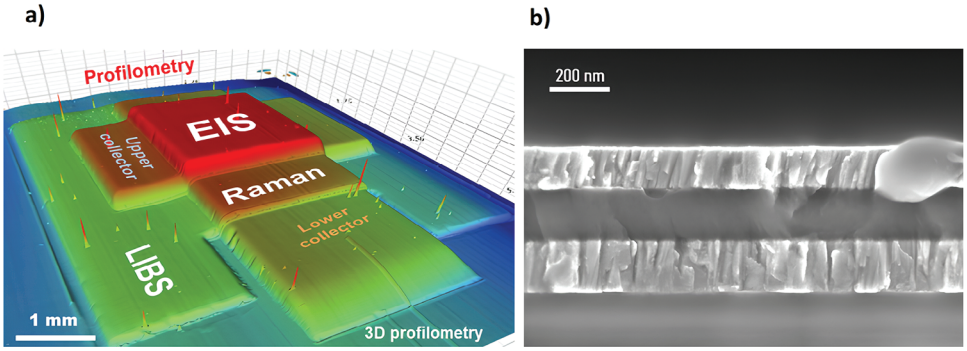

Figure 2. Microcell design: a) 3D rendering obtained by stylus profilometry showing the specific characterization areas, and b) Cr/$Li_xPO_yN_z$/Cr MIM stack at the centre of the microcell. SEM imaging of the Cr/LiPON/Cr stack was performed using a SEM-FEG (Zeiss, Sigma 500) equipped with an InLens detector, at a voltage of 10 kV and working distance of 5 mm. High-throughput characterizations.

such as hydrogen or lithium. However, specific developments are necessary to achieve quantitative analysis.[42] In addition, one advantage of this technique is that it does not require any special preparation of the sample.

2.2. Combinatorial Synthesis

Combinatorial synthesis of Li-P-O-N materials was carried out by reactive magnetron co-sputtering of lithium phosphate targets with different Li/P ratio in a plasma of pure nitrogen. This synthesis method was chosen for several reasons: (i) it is already used or envisioned for the preparation of actual battery components (with atomic layer deposition),[43,44] (ii) it should allow amorphous materials with a wide range of compositions to be prepared easily, (iii) compared to other approaches using magnetron sputtering such as sequential sputtering that alternate the deposition of sub-atomic layers or allow the preparation of material matrices using a set of shadow masks,[32,45] the present method does not require a specific, complex and fragile mechanical setup inside the chamber, leads to optimisation of the deposition rate, and does not require any thermal post-treatment. Co-sputtering from multiple targets to produce thin films with composition gradients spreading at the surface of a large substrate has been used for decades to generate material libraries, then to initiate high throughput screening of materials for many applications. But the simplicity of this process has a downside: it is not possible to accurately predict the composition and thickness of the material deposited at a specific point on the substrate. Consequently, these data must be measured after the deposition.

The sputtering device (Plassys, France) used for the preparation of LiPON libraries is connected to an argon-filled glovebox with less 1 ppm of oxygen and water. The design allows the chamber to be opened in the controlled atmosphere, preserving targets and films from contamination at all times. Co-sputtering was performed using only two targets from a group of three tiltable 2'' targets that are distributed at 120 ° intervals around a vertical axis coinciding with that of the substrate, positioned at one of four deposition locations available in the chamber. The distance (D) between the substrate plane and the centre of the target was set to 86.2 mm and each target was tilted at an angle (Θ) of 15.25 ° to allow for mixing of species originating from each target and to generate a composition gradient on the surface of the immobile 4'' substrate. Prior to deposition, the system was evacuated to a base pressure of 6.7×10^{-8} Pa. Co-sputtering was performed under pure N_2 at a working pressure of 1 Pa, applying powers of 3.65 W.cm^{-2} and 3.06 W.cm^{-2} to the Li_3PO_4 and $LiPO_3$ targets, respectively. Pre-sputtering was conducted for 30 min prior to actual film deposition.

2.3. Design and Preparation of Sample "Microcells"

The microcells (**Figure 2a**) have been designed to enable local application of the full set of characterizations to each of the 76 samples. The cells have been intentionally made small to ensure that the film composition can be considered homogeneous across the entire area, but large enough to complete the full set of analyses. In this regard, the 5×5 mm^2 format, which represents only 0.3% of the substrate area, was considered as a good trade-off. The microcell array is prepared on a single 4'' wafer (Si<100>/SiO_2/Si_3N_4) in three successive steps. First, a (bottom) chromium current collector is deposited, followed by LiPON, and finally a (top) chromium collector, each through a specific shadow mask. Chromium films have been deposited at 0.6 Pa and 3.06 W.cm^{-2} on a rotating substrate to ensure homogeneity of the metal thickness across the wafer area. As a result, the cell pattern provides suitable areas for conducting each of the characterizations (Figure 2a). The 2×2 mm^2 Metal-Insulator-Metal (MIM) stack, formed in the central part, is used to perform impedance spectroscopy (EIS) measurements. The thickness of the current collectors has been set to 200 nm, enabling EIS characterization of LiPON films with a thickness as low as 150 nm (Figure 2b). A 2 mm^2 area where the LiPON is deposited on Cr is used for Raman spectroscopy, while another 2 mm^2 area covered with plain LiPON is available for elemental analysis by LIBS. Finally, height profiling is performed across the LiPON pattern to determine the film thickness.

2.3.1. Stylus Profilometry

The thickness of the LiPON film present in each of the 76 cells is determined by automated stylus profilometry (Bruker,

DektakXT), using a tip radius of 12.5 µm and a tip force of 1 mg. Four profiles are measured over 2.5 mm for all microcells. The average of those measurements gives the thickness of the microcell, with an excellent repeatability (<5%). The automated mode of these profile measurements allows to probe 76 microcells in about 2.5 hours. Then, in order to assess microcell homogeneity in term of thickness, three-dimensional measurements are carried out on all samples. 3D-maps of on 6 × 6 mm^2 area shows a homogeneous thickness distribution with error of <5% within the microcell.

2.3.2. Laser Induced Breakdown Spectroscopy (LIBS)

A comprehensive description of the setup used for LIBS measurements has been reported by *Motto-Ros* et al.[46] In brief, the sample was analysed using a single shot of a 1064 nm – 8 ns – 0.8 mJ focused laser beam per location. This results in an ablation crater of ∼ 10 µm in diameter and ∼ 5 µm deep, therefore much deeper than the thickness of the LiPON film. Three different Czerny-Turner ICCD spectrometers enable to detect and analyse emission lines related to Li, P, and Si, so that three LIBS spectra covering three distinct spectral ranges are recorded simultaneously at a given XY location on the wafer. XY-translation stage enables scanning the sample surface with a 35 µm spacing. Automated characterizations allow a mapping of 5 × 5 cm^2 in 5 h. In this particular case, where we wanted to be able to combine LIBS and combined RBS and Nuclear Reaction Analyses (NRA) to validate the technique, a specific deposition was used to obtain thin layers with a thickness in the range of 100–200 nm. It was carried out in exactly the same way as for microcells, with the difference that the deposition time was reduced to 1 hour. Note that we concluded in an earlier study that quantitative LIBS analysis is possible for film thickness up to 700 nm.[42]

2.3.3. Raman Spectroscopy

Raman spectroscopy, which can reveal the presence of different phosphate structural units, was used in automated mode to probe the local structure of the amorphous LiPON materials, using a confocal Raman spectrometer (Horiba, LabRAM Odyssey). The latter was equipped with a x50 lens and a 633 nm, 17 mW laser. This wavelength was selected to reduce sample fluorescence. Acquisition lasts for 600 s with two scans within the 500–1400 cm^{-1} range, at a spacing of 1.14 cm^{-1}. The focus was manually set on each microcell before running the automated mode. Automated acquisition allows 76 microcells to be scanned in approximately 24 hours. The measurements were finally carried out in ambient atmosphere, as no change in the LiPON spectrum was observed even after 7 days of exposure to air.

In order to get clear overview on Raman spectra, luminescence is removed by a baseline function, (Asymmetric Least Square Smoothing), using 0.05 threshold, 6 as smoothing baseline coefficient and 50 iterations. OriginLab software is used. Those parameters are chosen to avoid intensity alteration of all peaks, in order to fit each spectrum with the smoothest baseline.

2.3.4. Electrochemical Impedance Spectroscopy (EIS)

EIS measurements have been carried out at room temperature inside an Ar-filled glove-box using a VMP3 galvanostat –potentiostat-impedancemeter (Biologic, France) and shielded micro-probes for connecting the cells. They were performed in the 50 Hz to 400 kHz frequency range using a voltage amplitude of 50mV_{ac}. Repeatability of the EIS measurements has been checked over several cells. The standard deviation of values related to functional properties (σ_{Li+}, n_{Li+}, ϵ_{LiPON}) has been calculated from the results of the four thickness measurements carried out on each sample and the estimated error associated with each component of the fit, as provided by the EC-lab software. All Nyquist plots showed excellent repeatability. Plots were then fitted using the Z fit toolbox embedded in the EC-lab software to extract some intrinsic properties of the LiPON materials:

- The ionic conductivity (σLi+), calculated from equation 1.a where d is the solid electrolyte thin film thickness, A the area of the electrode and R the solid electrolyte thin film resistance deduced from the Nyquist diagram,
- The dielectric permittivity (ϵr) of the material,[47] calculated from equation (1).b, where ϵ0 is the vacuum dielectric constant, CLiPON is the capacitance and d the thickness of the solid electrolyte thin film, A the overlap area of the two chromium current collector,
- The Debye Length LD is calculated from CLiPON which the capacitance of the solid electrolyte, the capacitance of the solid electrolyte/blocking electrode interface Celectrode and d the thickness of the solid electrolyte thin film,
- The charge carriers density (nLi+),[47] calculated from equation 1.d where ϵ0 is the vacuum dielectric constant, ϵr is the dielectric constant of the solid electrolyte, T is the room temperature, kB the Boltzmann constant, q is the elementary charge of one electron and finally LD the Debye length. In order to calculate charge carrier concentration, equation (1).b and (1).c are used.

$$\text{a) } \sigma_{Li+} = \frac{d}{A \times R_{LiPON}} \quad \text{b) } \epsilon_r = \frac{C_{LiPON}}{\epsilon_0}\frac{d}{A} \quad \text{c) } \frac{C_{electrode}}{C_{LiPON}} = \frac{d}{2L_D} \quad \text{d) } n_{Li+} = \frac{\epsilon_r \epsilon_0 T k_B}{q^2 L_D^2} \quad (1)$$

Effective capacitances C_{LiPON} and $C_{electrode}$ are calculated from the Constant Phase Elements Q_x which corresponds to the bulk material or to the two electrode interfaces respectively, according to the equation $C_x = (Q_x R_{LiPON}^{1-\alpha_x})^{\frac{1}{\alpha_x}}$. The terms of this equation depends on *x*, taking *"LiPON"* or *"electrode"* as meaning. Other terms used are C_x the effective capacitance considered, R_{LiPON} the solid electrolyte thin film resistance, Q_x the Constant Phase Element (CPE) and α_x a factor to describe the diverging behavior of a CPE from an ideal capacitance.

2.4. Additional Characterizations

2.4.1. Chrono-Amperometry (CA)

Electrical measurements were conducted on microcells using chronoamperometry to determine the electronic conductivity of the LiPON materials with the same setup used for EIS measurements. The current evolution was recorded for 10 hours while

Table 1. Summary of all characterizations performed on dedicated wafers.

Category	Techniques	Deposition time	Substrates
High Throughput	Stylus profilometry	8h	Microcells on $Si_3N_4/SiO_2/Si$ wafer
	EIS		
	Raman		
	LIBS	1h	Microcell patterns w/o current collectors on $Si_3N_4/SiO_2/Si$ wafer
Complementary techniques	SEM	8h	Microcells on $Si_3N_4/SiO_2/Si$ wafer
	Chronoamperometry		
	ICP-OES		22 PTFE discs (15 mm ø) arranged on a wafer
	RBS / NRA	1h	7 glassy carbon (6 mm ø) placed over $Si_3N_4/SiO_2/Si$ wafer

applying a voltage difference of 100 mV_{dc} on the cells. As previously described in EIS characterization method, the same setup is used for chronoamperometry, at room temperature in order to probe electronic conductivity. Due to time constraints, these measurements were performed only on three microcells which locations correspond to the two extreme compositions and a median composition between them. The electronic conductivity (σ_{e-}) is calculated from equation (2) where d is the solid electrolyte thin film thickness, I_{res} the residual current, A the overlap area of the two chromium current collector and U is the applied voltage.

$$\sigma_{e-} = \frac{d.I_{res}}{A \times U} \quad (2)$$

2.4.2. Rutherford Backscattering Spectroscopy (RBS) and Nuclear Reaction Analysis (NRA)

The elemental composition of $Li_xPO_yN_z$ was determined using Nuclear Reaction Analysis (NRA) and Rutherford Back Scattering spectrometry (RBS) on a 3.5 MV Singletron, HVEE, accelerator (AIFIRA Facility).[48] RBS analysis was performed with 2.0 MeV alpha ions ($^4He^{2+}$) at a backscattering angle of 160° with a PIPS detector (Canberra) on samples deposited on diamond-polished glassy carbon (Sigradur G, HTW, Germany). The quantification of P, O and N contents was achieved, followed by the determination of the lithium content using the $^7Li(p,a)\,^4He$ nuclear reaction with a 2.906 MeV proton beam. A 133 nm thick LiF film prepared by evaporation on a silicon wafer was used as a calibration standard. For both measurement, the incident beam was circular with a diameter of 1 mm. The detector is set up at 53 mm from the sample, with an aperture of 5.7 mm. Its solid angle is of 9 msr. The current of the beam was around 10 nA for a dead time below 1%. Charge was integrated during measurement with a dedicated pico-amperometer. Data were processed using SimNRA software 7.03.

2.4.3. Inductive Coupled Plasma – Optical Emission Spectroscopy (ICP-OES)

Li and P contents and their distribution over the wafer were determined using Inductive Coupled Plasma – Optical Emission Spectroscopy (ICP-OES) (Agilent ICP/OES 5800 DV). Since ICP-OES analysis involves dissolving the film sample, it was necessary here to deposit it on PTFE discs (diameter 15 mm) arranged at regular intervals on the wafer. The deposition was carried out in the same way as for the microcells. Twenty-two discs were positioned and attached on the wafer using double-sided Kapton tape at the location of every second cell. The thin films deposited on PTFE discs were dissolved in 2.5 ml HCl + 2.5 ml HNO_3, filled up to 30 ml with deionized water. For each ICP sample, characterization was performed five times. The emission lines used were Li I 670.79 nm and P I 214.91 nm (**Table 1**).

3. Results and Discussion

3.1. The LiPON Library

Since the geometry of the spraying system and the total nitrogen pressure have been set, the conditions for mixing the elements sputtered from the two targets ($LiPO_3$ and Li_3PO_4) remain conditional on the powers applied to each of them. Deposition rate gradients were assessed separately at different powers for both targets. Sputtering conditions were then chosen to combine similar and sufficient rates. Application of 60 W to the $LiPO_3$ target and 70 W to the Li_3PO_4 target were found to be suitable, resulting in maximum deposition rates of 203 $nm.h^{-1}$ and 208 $nm.h^{-1}$ and contrast ratios of 40/1 and 20/1 respectively. **Figure 3**a,b show the distribution of deposition rates across the wafer, highlighting the location of the maximum values close to each target. Using these conditions to prepare the library of 76 samples by co-sputtering then results in a film thickness distribution with two maxima in the vicinity of the two targets (Figure 3c,d), which should logically be accompanied by a continuous variation in composition across the wafer. At this stage, comparison of the deposition rates for separate deposition and the co-deposition experiments shows that this process can be considered as approximately additive. However, such a hypothesis regarding the composition of films remains to be established.

3.2. Mapping the Functional Properties

As shown in Figure 3c, a deposition time of 8 hours under these conditions resulted in a film thickness greater than 500 nm for

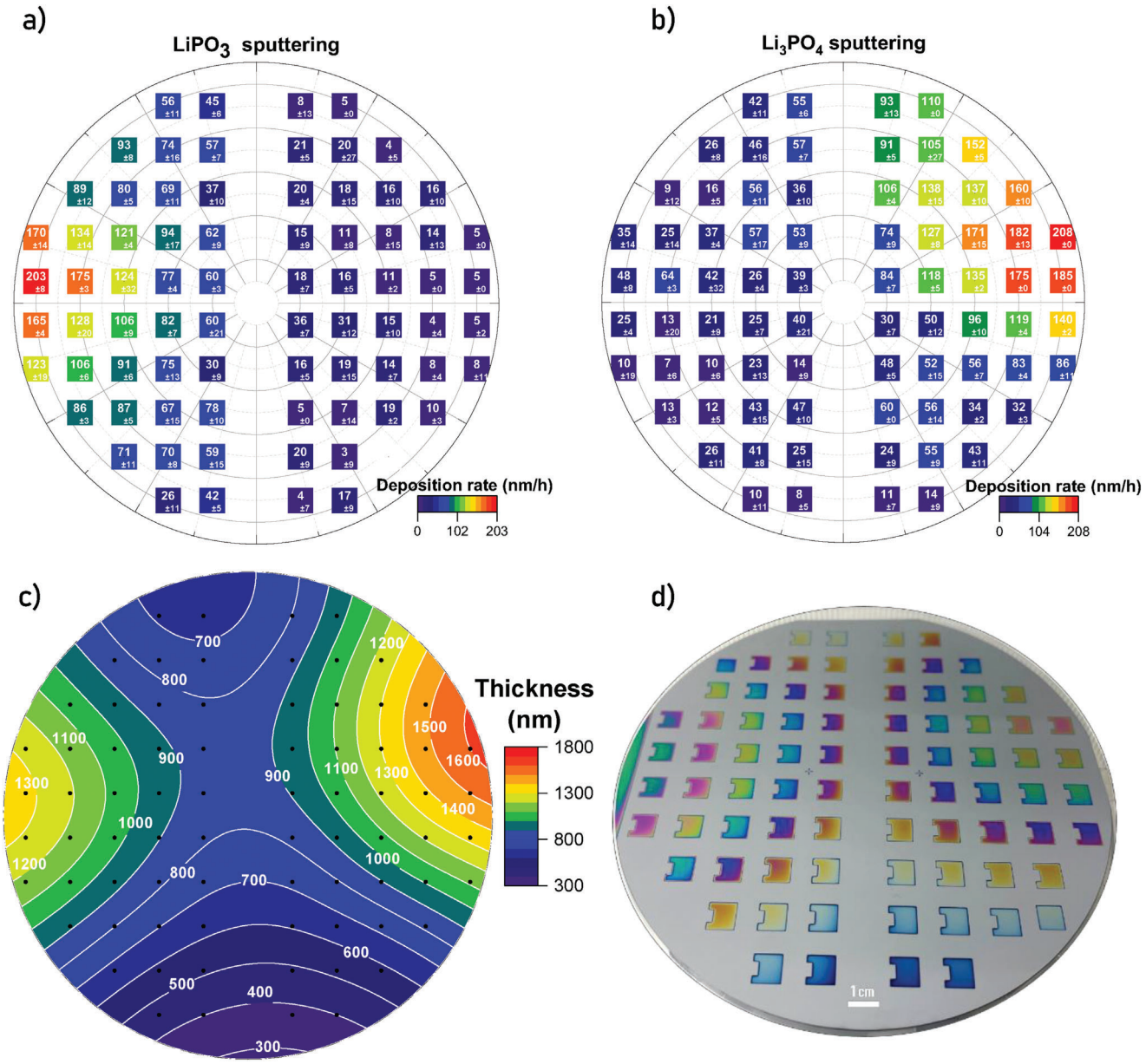

Figure 3. A & b) Local deposition rates measured by stylus profilometry for separate depositions from the tilted $LiPO_3$ target and Li_3PO_4 target, at 60 W and 70 W respectively, c) distribution of film thickness over the wafer after 8 h co-sputtering of $LiPO_3$ and Li_3PO_4 targets displayed as a contour plot using interpolation of measurements over the 76 samples (raw values are provided in Figure S1), d) photograph of the corresponding wafer, where the variation in color reveals the variation in thickness.

92% of the cells and a thickness of 352 nm for the thinnest sample. These values are considered sufficiently high to ensure reliability and accuracy for measuring the electrical properties of the deposited films embedded in MIM microcells, between ion blocking Cr electrodes. Characterization of ionic conductivity, relative permittivity, mobile charge carrier concentration and electronic conductivity were then carried out using impedance spectroscopy and chronoamperometry in an Ar-filled glove box, and for the moment, only at room temperature. These features are indeed of particular interest, although not the only ones, for the envisaged applications of these materials. EIS measurements, carried out successively on each of the 76 cells, were completed in 4 h. **Figure** 4a shows some Nyquist plots obtained from different cells, which are therefore dependent on both the composition and thickness of the sample under consideration.

Each spectrum has been fitted using an R1-(CPE2//R2)-CPE3 electrical circuit for representing the MIM stack, where R1 is the resistance of the external electrical circuit, CPE2//R2 accounts for the LiPON electrical response, and CPE3 is the non-ideal capacitance resulting from charge accumulation at the Cr/LiPON interface at low frequencies. The refinement of all plots resulted in minimal residuals, while the constant phase elements CPE2

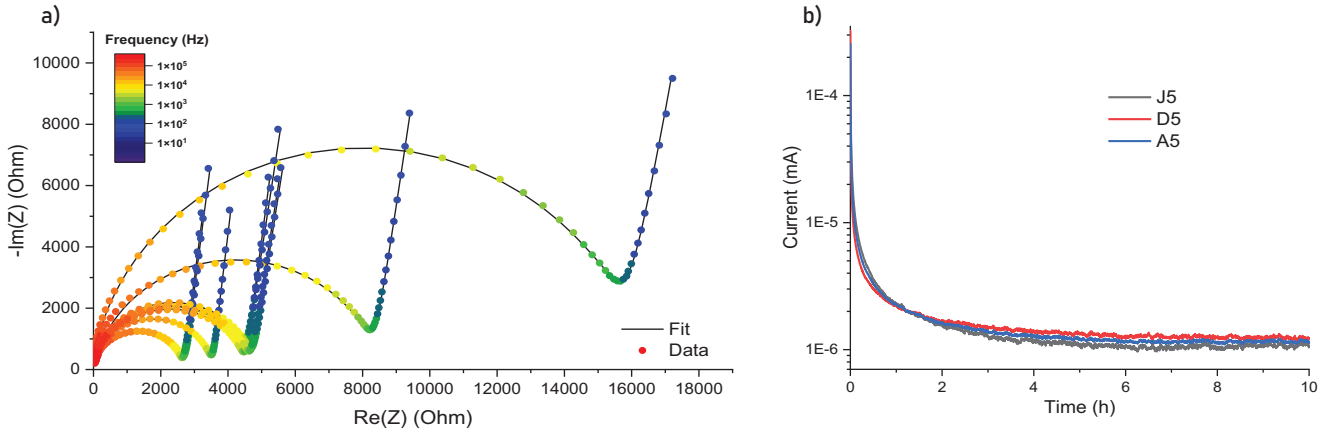

Figure 4. a) EIS plots of various MIM microcells displayed as Nyquist plots, b) chronoamperometry curves for three cells located in the vicinity of each target and near the center of the wafer. All measurements were performed at room temperature in an Ar-filled glove box.

and CPE3 were found to be close to ideal capacitances with α_2 and α_3 values in the range 0.89-0.95.

The ionic conductivity σ_{Li+} of each sample has been calculated from the value of the R2 resistance, the thickness of the LiPON film and the active surface area of the corresponding MIM microcell. Finally, this data treatment consistently reveals a continuous gradient spreading over the whole surface of the wafer (**Figure** 5a), with ionic conductivity values varying between 0.14(1) and 1.34(1) $\mu S.cm^{-1}$. The latter value is in accordance with data reported for conventional LiPON materials, such as $\sigma_{Li+} = 1.8(1)\ \mu S.cm^{-1}$ for $Li_{3.2}PO_{3.5}N_{0.25}$.[49] Furthermore, as values increase in proximity to the Li_3PO_4 target, it is likely that lithium content is the primary factor affecting conductivity of the material.

Determining the concentration of mobile charge carriers (n_{Li+}) provides additional information regarding this overall trend. n_{Li+} can be calculated using equations 1, with intermediate determination of the relative permittivity and the Debye length. Plotting ionic conductivity as a function of concentration reveals two distinct domains (Figure 5b). The first domain corresponds to a gradual increase in conductivity over almost a factor of ten as the concentration rises from around $1.10^{25}\ m^{-3}$ to around $8.10^{25}\ m^{-3}$. The second shows a stabilization of the conductivity beyond this point, at around 0.8-1.0 $\mu S.cm^{-1}$, even for concentrations reaching a much higher level. Note that a similar behavior has been reported for the LiSiPON system, in which the conductivity was levelling for Li/(P+Si) contents higher than 1.[26]

Based on the combined observation of this trend and the location of the samples, it can be assumed that the mobile carrier concentration is primarily influenced by the Li content in the film and that the increase of the mobile charge carrier above a certain value induces a decrease of the charge carrier mobility. This probably highlights the transition between the behavior of a weak electrolyte in which Li+ ions can move independently of each other,

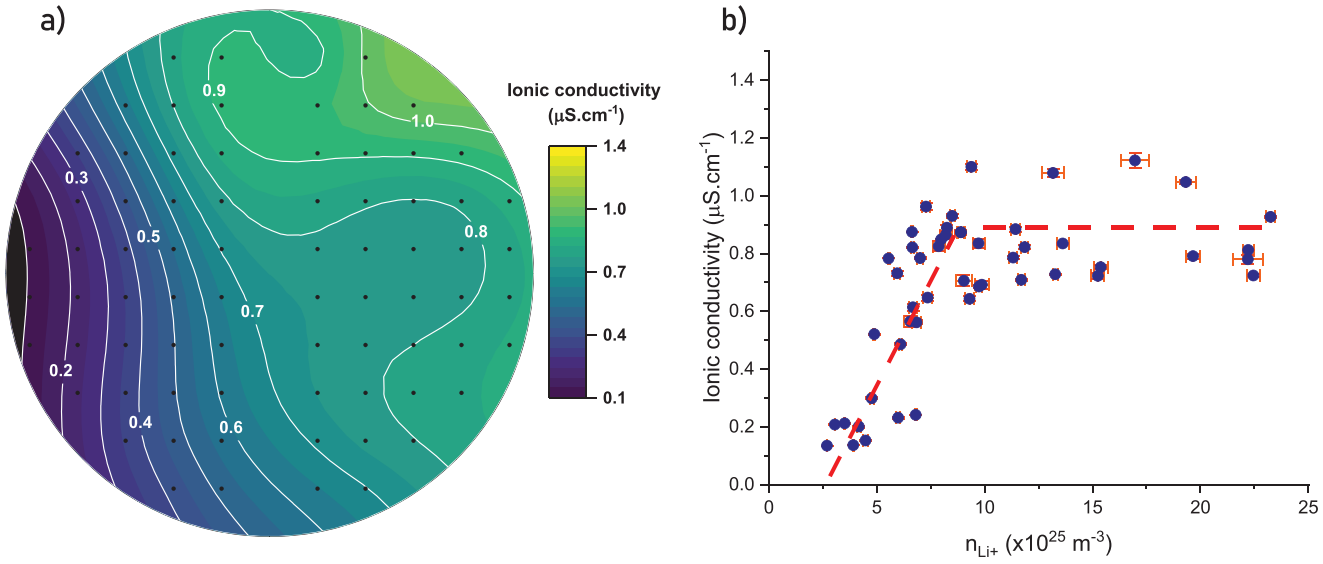

Figure 5. a) spatial distribution in ionic conductivity displayed as a contour plot (raw values are provided in Figure S2), b) trend of the ionic conductivity as a function of the mobile charge carrier density.

Table 2. Electronic conductivity and leakage current of selected samples.

Cell	A5	D5	J5
Thickness (nm)	1469 (63)	845 (38)	1601 (15)
σ_{e^-} (x10^{-11} S.cm^{-1})	4.0 (1)	2.6 (1)	4.7 (1)
Electric field applied (kV.cm^{-1})	0.7	1.2	0.6
Leakage current (nA.cm^{-2})	27	31	29

and that of a concentrated electrolyte in which the movement of these ions is necessarily coordinated and accompanied by a rearrangement of the structural units within the network.[50] Significant variations in nitrogen content can also strongly influence the concentration of the mobile charge carriers independently of Li content,[49] but can only be generated by significant variations in reactive sputtering conditions. In this case, since these conditions are fixed, the variability of the nitrogen content in the samples and its effect on the charge carrier concentration should remain moderate.

Besides, no particular trend was observed for the relative permittivity ϵ_r or dielectric constant κ which remain within the [37–47] range for all cells (Figure S3), showing that LiPON is a high-κ material across a wide compositional range.[51] Additional information regarding complex permittivity are provided in Figure S4 and Table S1.

In most applications, such as microbatteries and microsupercapacitors, electronic transport is detrimental to the performance of LiPON as it leads to self-discharge of the component. Therefore, it is necessary to minimize electronic conductivity relative to ionic conductivity. This parameter (σ_{e^-}) has been measured by chronoamperometry (Figure 4b) on three cells corresponding to the Li-poor region *(A4)*, the Li-rich region *(J4)* and an intermediate composition *(D4)* as well as calculated using the value of the residual (or leakage) current and equation 2. The three values were similar (**Table 2**), which seems to show that the Li/P ratio has little influence on the electronic conductivity and were four to five orders of magnitude lower than the ionic conductivity.

3.3. Chemical Mapping of the LiPON Library

As previously mentioned, achieving fast and spatially-resolved chemical analysis of thin films containing light elements is a challenge that we aim to address using Laser-Induced breakdown Spectroscopy. In fact, two approaches can be used to assess the technique. The first is a conventional method that requires calibration by comparing results with those obtained from other quantitative techniques. The second one is based on a calibration-free method that proceeds via a mathematical fitting of full spectra by calculating the population densities present in the plasma under the same conditions.[52,53] At this stage of the development of the HTE approach, we chose to rely solely on the first one and carry out series of thin film analyses by ICP-OES, RBS and NRA, in addition to LIBS.

3.3.1. Chemical Mapping by ICP-OES, RBS and NRA

ICP-OES analyses were conducted on 22 samples arranged across the whole surface of the substrate to determine individual Li/P ratios and their spatial evolution. Since the PTFE substrates are 15 mm in diameter, they could be arranged side by side on the wafer at a position centered on every other microcell. Therefore, the compositions assigned to microcells located in between were calculated using linear interpolation. These analyses show a gradient of Li/P spreading across the wafer and was achieved in the range from 0.92 to 2.05. The distribution of this ratio which is displayed on a contour map (**Figure 6**) is consistent with the relative positions and compositions of the targets. What was less expected is that the highest value of 2.05 achieved close to the Li_3PO_4 target and is significantly lower than 3. This difference, generated during the sputtering process, can have different origins such as different sputtering yields between Li and P, different angular distributions of the sputtered species and/or different sticking properties on the substrate. These effects cannot be known precisely beforehand; however they could be compensated for afterwards by changing the composition of the target. In this case, it simply means that the compositional domain studied is narrower than the one targeted.

Rutherford Backscattering Spectrometry (RBS) and Nuclear Reaction Analysis (NRA) are two well-known ion-beam characterization techniques for studying the chemical composition of thin films.[54] While the former allows to characterize elements with atomic mass higher than beryllium, thanks to elastic scattering of He^{2+} particles, it fails to detect light elements such as Li. This is why a usual coupling of both techniques is used to quantify all elements except hydrogen, which is thereby calculated. These analyses require the use of a large instrumental facility and therefore cannot be carried out routinely.

The RBS and NRA analyses were carried out on a limited number of glassy carbon discs placed in the vicinity of selected microcells. Co-deposition was performed simultaneously on these discs and on microcells, allowing combined LIBS, RBS and NRA analyses to be performed on the same library. Compared to ICP-OES, the aim was to achieve a complete quantitative analysis of some samples, i.e., to determine the Li, P, O, N stoichiometry.

Figure 7a shows the RBS spectrum of a LiPON thin film deposited on glassy carbon with the associated fit, where O, P and N contributions are well resolved and separated. The fitting of the spectrum allowed to determine the N, O, P contents. The results, reported in Figure 7b, show in particular that all the samples distributed on the surface contain a high amount of nitrogen with an N/P ratio of between 1.00 and 1.22. Thus, the variation in the N/P ratio over the surface of the wafer appears to be relatively moderate compared with that of the Li/P ratio. Therefore, it can be assumed that the change in properties between the different samples synthesized on this wafer will be primarily influenced by the lithium content.

Coupled NRA-RBS analyses were performed on 3 samples *A5, J4, D4* that again correspond to Li-poor, Li-rich and intermediate compositions. The Li/P values obtained from combined fitting of the spectra were found to be 0.95, 2,03 and 1.45 respectively, and are therefore in very good agreement with the ratio provided by ICP-OES. Figure 7d illustrates the expected trend of a gradual increase in the (O+N)/P ratio as a

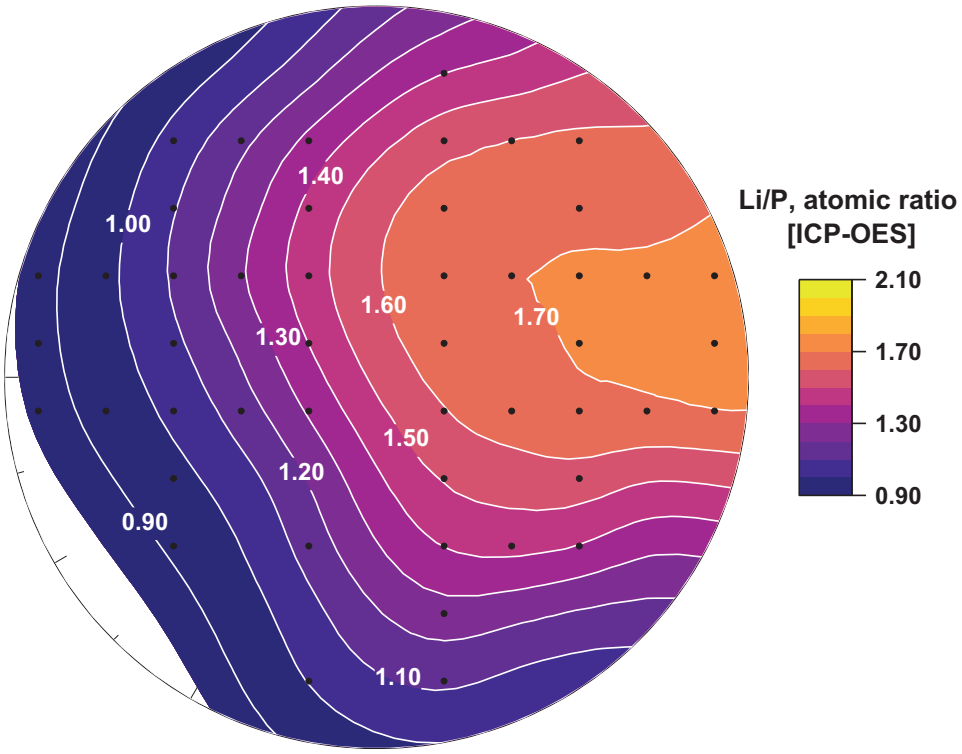

Figure 6. Distribution of the Li/P ratios determined by ICP-OES (raw values are provided in Figure S5).

function of Li/P content, while the nitrogen content appears to remain approximately constant and at a high level.

Incidentally, a particular concern was revealed by these analyses. Indeed, while it could be assumed that the Li content x in $Li_xPO_yN_z$ can be calculated using the formula x+5-2y-3z = 0 which represents the charge neutrality relationship, Li/P values obtained this way from the sole RBS analyses were found to be always slightly higher (+0.2-+0.4) than the values provided by combined NRA/RBS or ICP-OES analyses. At the same time, it was found that the contribution of hydrogen in the film had to be taken into account to improve the refinements. These two pieces of information work together to confirm the presence of hydrogen inside the films, which therefore have the actual $Li_xPO_yN_zH_w$ formula. Note that to our knowledge, it is the first time that this point has been recorded in LiPON films. The way hydrogen is introduced in the films is not yet identified. It could originate from air exposure of the ceramic target, which is never 100% dense, prior to installation in the equipment. A specific study, using Elastic Recoil Detection Analysis (ERDA) for example, will be required to directly confirm the presence or absence of hydrogen in the films, and then determine its possible influence on the material's properties.

3.3.2. Assessment of LIBS for a Quantitative Chemical Mapping

LIBS analyses were performed at first on the same $Li_xPO_yN_z$ films or on samples that were previously examined by combined RBS+NRA (100-200 nm). The acquisition was performed at 100 Hz on the samples, meaning that 100 LIBS analyses were achieved per second on 100 distinct locations of the microcell (using a 35 µm spacing, 1 mm^2 is scanned in 8 s, generating 800 spectra). The spectra recorded simultaneously in three spectral domains are displayed in **Figure** 8a–c. Peaks attributable to the different elements present in the film, substrate and surrounding atmosphere are clearly visible: Si (I) & (II), Li (I), P (I), and even H (I). Note that the presence of H could confirm the observations made earlier. Signal-to-Noise Ratio (SNR) is excellent for all major peaks, i.e., Si (I) 205, 212, 221 nm; Li (I) 413, 460, 610, 670 nm; P (I) 214 nm, and even H (I) 656 nm. Several emission lines may be suitable for quantitative analysis regarding Li and P. However, careful examination is necessary to avoid the influence of possible self-absorption or saturation phenomena. Figure 8d displays the evolution of the LIBS signal intensity of different lithium lines along the Li (I) 610 nm. Linear trends are observed for Li (I) 460 nm and Li (I) 413 nm, while it is not the case for the Li (I) 670 nm line. This observation is attributed to the saturation of the LIBS signal above 4.00×10^5 counts. Therefore, only Li (I) 610, 460 or 413 nm lines can be used for quantification purposes. As for phosphorus, the P (I) at 214 nm emission line, which is also used in ICP-OES, was chosen.

In order to assess potential matrix effects, LIBS analyses were performed on microcells deposited on both the silicon wafer and on films deposited on glassy carbon disks placed at almost the same positions. Films on carbon disks were also analyzed by RBS+ NRA. For both substrate materials, the plot (**Figure** 9a) of the LIBS intensity ratio $Li_{610\,nm}$ / $P_{214\,nm}$ as a function of the Li/P composition determined by RBS+NRA shows a good correlation ($R^2 > 0.98$) between the respective values

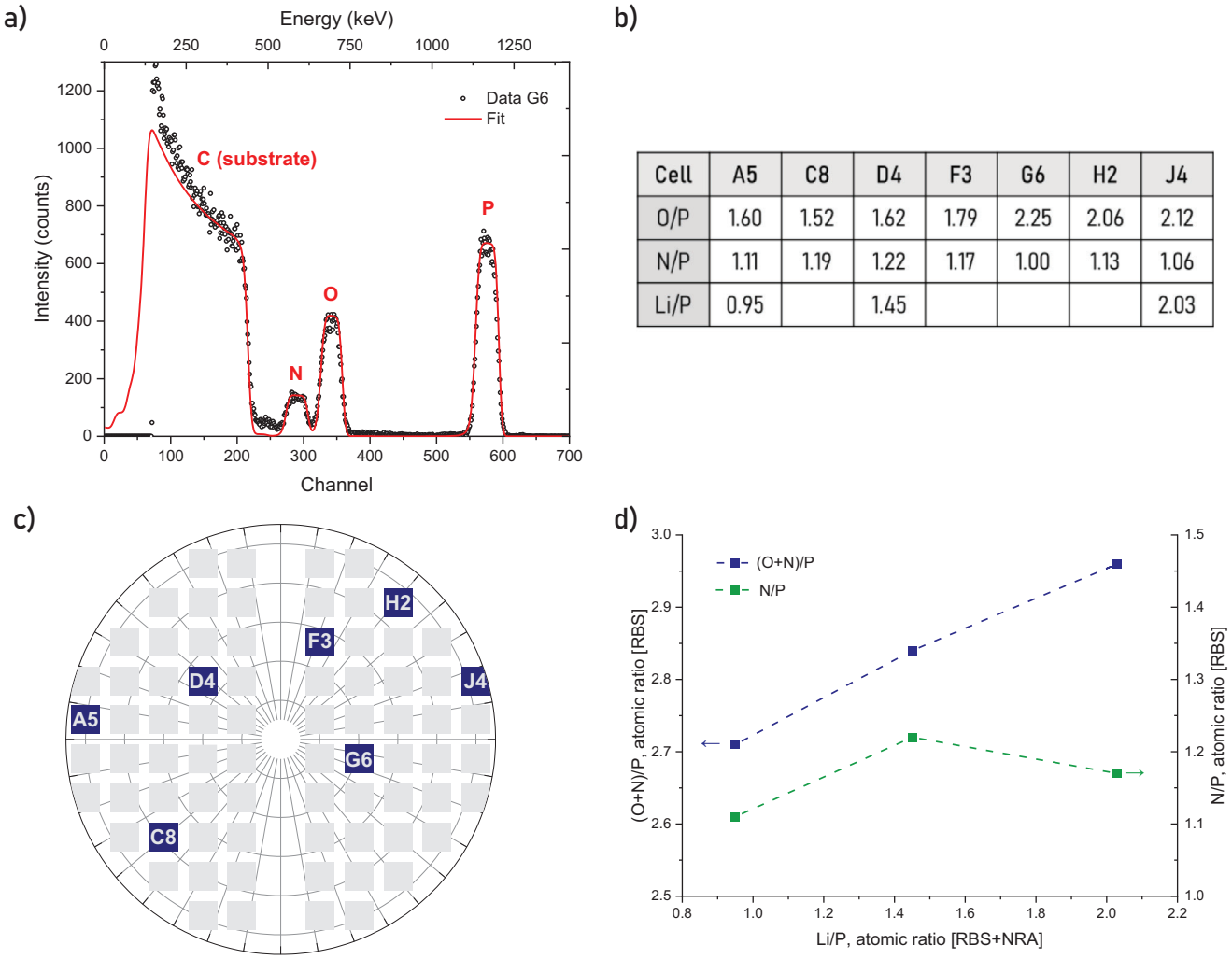

Cell	A5	C8	D4	F3	G6	H2	J4
O/P	1.60	1.52	1.62	1.79	2.25	2.06	2.12
N/P	1.11	1.19	1.22	1.17	1.00	1.13	1.06
Li/P	0.95		1.45				2.03

Figure 7. a) Example of an experimental RBS spectrum and its associated fit, b) compositions of seven cells distributed on the wafer obtained by NRA and/or RBS, c) position of these samples on the wafer, d) (O+N)/P and N/P as a function of Li/P, obtained from coupled RBS and NRA analyses on three samples.

over the Li/P range from 0.95 to 2.03. This calibration made it possible to use LIBS to map the Li/P ratio quantitatively over the entire wafer. Due to limited access to the equipment, the mapping was conducted based on the analysis of only 20 samples. The corresponding contour map, which includes interpolation between experimental data, is shown in Figure 9b. Although the analysis was carried out on a limited number of cells, there is a good match between the mappings performed by ICP-OES and by LIBS in terms of both values and their distribution.

At this stage, only the chemical data related to Li and P have been used. Emission lines of oxygen, nitrogen and hydrogen can also be measured. However, since LIBS analyses are carried out in ambient air with just a flow of argon directed towards the ablation zone, the possibility that some of the species analyzed may have come from the environment cannot be ruled out. A modification of the setup is therefore necessary to assess the possibility of carrying out quantitative analyses of the other elements present in LiPON.

3.4. Local Structure of LiPON Materials

The structural network of amorphous LiPON results from the arrangement of $P(O,N)_4$ tetrahedral units. This arrangement depends mainly on the overall (O+N)/P ratio, which is itself highly dependent on the Li/P ratio and on the method of preparing the material. In relation to this, material synthesis by sputtering, which consists of depositing elementary species at room temperature, is likely to lead to more disordered materials than the melting/quenching preparation method where entities are more likely to organize themselves. The structure of phosphate with a low Li content (Li/P ~ 1) is mainly based on the arrangement of tetrahedral units that share two bridging oxygen to form semi-infinite linear chains. When nitrogen is introduced into these materials, it induces the formation of oxynitride units (PO_3N or PO_2N_2) that share either a doubly (P-N = P) or triply coordinated (P-N<P_2) bridging N.[16,55] As for materials with a high Li-content (Li/P ~ 3), there is a consensus on the presence of mainly $P_2O_7^{4-}$ or PO_4^{3-}, $P_2O_6N^{5-}$ or $P_2O_5N_2^{6-}$ separate units. Therefore, only

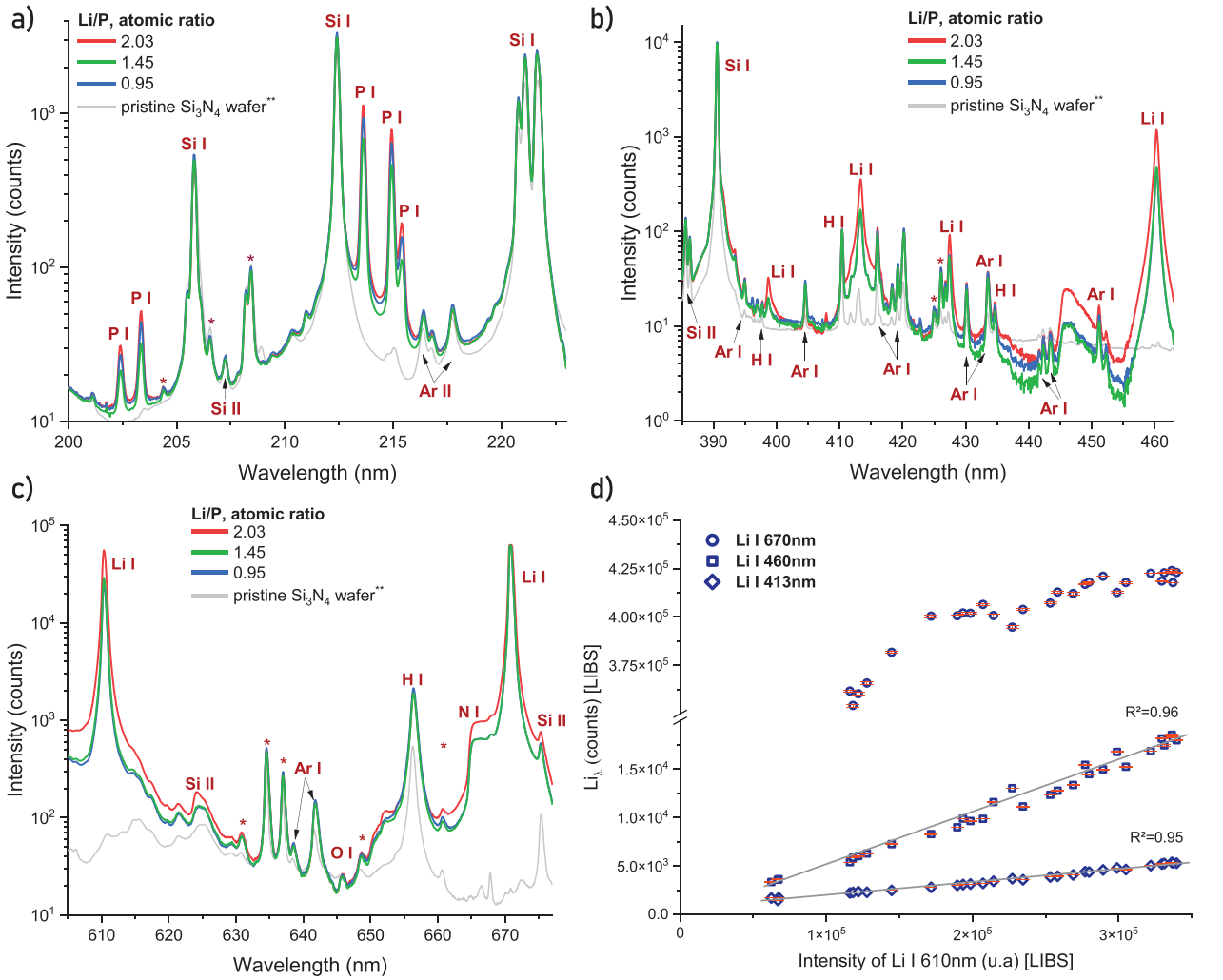

Figure 8. LIBS signals of three cells of the library prepared on the $Si_3N_4/SiO_2/Si$ wafer, in different spectral ranges a) 200–225 nm, b) 385–465 nm and c) 590–690 nm, d) evolution of the intensities of three lithium lines as a function of that of the standard Li (I) 610 nm line. Atomic ratios were scaled using RBS/NRA results. ** Grey lines correspond to the contribution of a bare $Si/SiO_2/Si_3N_4$ wafer measured in a separate experiment.

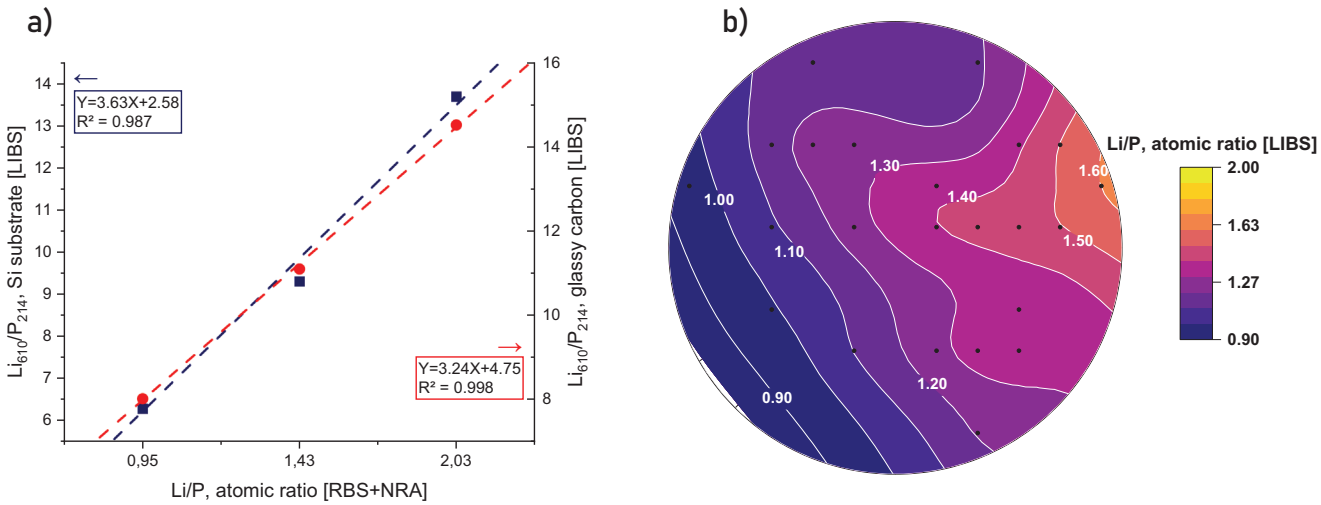

Figure 9. a) Correlation of the Li_{610}/P_{214} intensity ratio from LIBS with the Li/P atomic ratio determined by ICP-OES, b) Spatial distribution of the Li/P atomic ratio obtained from LIBS analysis of 20 samples and subsequent calibration.

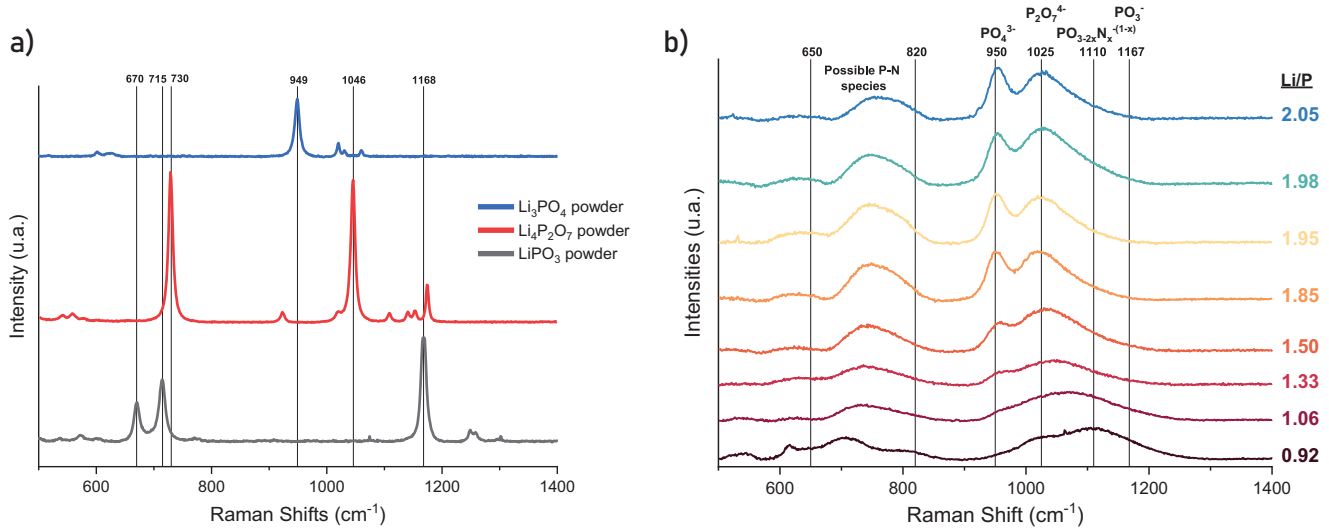

Figure 10. Raman spectra of a) lithium (ortho-, pyro-, meta-) phosphate powders (see Figure S6 for corresponding XRD patterns), and b) $Li_xPO_yN_z$ films of the library in with x ranging from 0.92 to 2.05.

apical ($O_3POPO_2N^{5-}$) or bridging ($O_3PNPO_3^{5-}$) nitrogen species are present in this case.[49,56,57]

3.4.1. Mapping the Library by Raman Spectroscopy

Raman spectroscopy is well suited for the structural analysis of these amorphous materials since it can reveal the different phosphate building blocks present in the materials. Additionally, automated measurements are already possible on some equipment. In order to unveil the expected vibrational modes for oxide-building blocks such as PO_3^-, $P_2O_7^{4-}$ or PO_4^{3-}, bulk crystalline $LiPO_3$, $Li_4P_2O_7$ and Li_3PO_4 were analyzed as reference materials (**Figure 10a**). The $LiPO_3$ spectrum exhibits the main vibration modes at 670, 715 and 1167 cm^{-1}. The two first ones are assigned to the symmetric stretching of P-O-P bonds, ν_s(P-O-P), and the latter to the asymmetric stretching, $\nu_{as}(PO_3^-)$.[58,59] The $Li_4P_2O_7$ exhibits the main vibration mode $\nu_s(P_2O_7^{4-})$ at 1025 cm^{-1}.[5,18,60] Finally, the Li_3PO_4 spectrum shows a main contribution at 949 cm^{-1}, attributed to the ν_s(P-O) vibrational mode.[5,60,61] These main contributions serve as a reference for the study of amorphous thin films using Raman spectroscopy.

High throughput Raman characterization was carried out on the 76 samples using an automated procedure. Figure 10b shows the Raman spectra of selected samples arranged according to their Li/P ratio determined by ICP-OES and highlighting the gradual evolution of the level of condensation of the structural units. The Raman shifts range is restricted to 500–1400 cm^{-1} in order to observe the phosphorus environment. N-compounds that are often tabulated around 700 cm^{-1} or 2000 cm^{-1}, are not detected here. The main peaks are observed within the 650–820 cm^{-1} and 940–1200 cm^{-1} ranges.

An overview of all spectra clearly shows three peaks at 950, 1025 and 1110 cm^{-1} with a possible additional contribution at 1167 cm^{-1}, if we refer to the spectrum of the $LiPO_3$ powder. In addition, at least three contributions appear in the range 650–820 cm^{-1}. The different contributions were assigned based on literature and the Raman spectra of the reference powders (**Table 3**). The major contribution of each structural unit at the given Raman shift was considered, while the contribution of the others was neglected. There are still uncertainties about the origin of the peak at 1110 cm^{-1} and the contributions in the 620–820 cm^{-1} range. *Pichonat* et al. assigned a PO_3^- vibrational modes at 1146 cm^{-1} for their LiPON thin films.[61] The incorporation of nitrogen in the film is likely to shift the PO_3^- vibrational modes. However, it is unclear whether this highlights an actual shift of the PO_3^- vibration or reveals the vibration of (PO_2N_2) oxynitride units as depicted by *Marchand* et al. for oxynitride lithium metaphosphate glasses.[55] With regard to the 620–820 cm^{-1} range, studies published in the literature concerning lithium-rich films suggest that nitrogen-containing species have contributions in this range,[5,18,60,62,63] as it is the case with $Li_{3.2}PO_{3.0}N_{1.0}$.[62] It is also the case for some PO_3^- vibrational

Table 3. Assignments of vibrational modes of $Li_xPO_yN_z$ thin films.

Vibrational mode (cm^{-1})	Attributed building block	Attributed with powder analysis	Refs.
650 – 820	PO_3^- or N-species	Partially	[5,18,58,60,63]
950	PO_4^{3-}	Yes	[5,60]
1025	$P_2O_7^{4-}$	Yes	[5,60,61]
1110	/	No	[61]
1167	PO_3^-	Yes	[58,59,64]

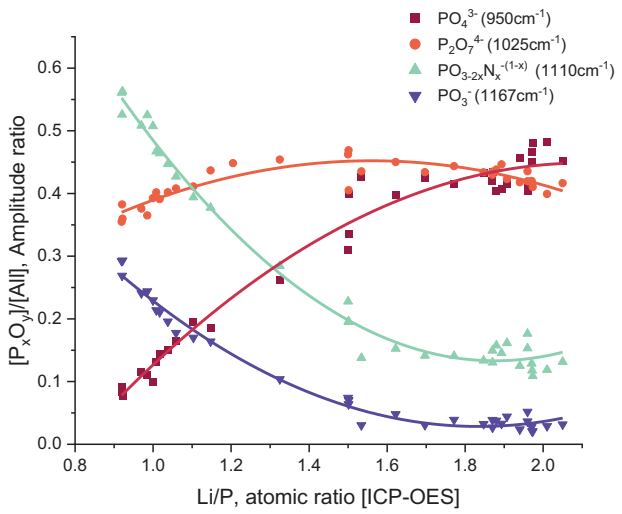

Figure 11. Qualitative overview of the evolution of the population of the different structural units as a function of the Li/P composition based on the amplitude ratios.

modes, as shown by the spectrum of the $LiPO_3$ powder. Consequently, the information contained in this area cannot be used for identifying specific structural features and will not be further considered.

Ultimately, the study of the whole $Li_xPO_yN_z$ library focused on the evolution of three main characteristic peaks at 950 cm^{-1} ↔ PO_4^{3-}; 1025 cm^{-1} ↔ $P_2O_7^{4-}$; 1167 cm^{-1} ↔ PO_3^-, and the unassigned contribution at 1110 cm^{-1}, labelled as $PO_{3-x}N_x^{-(1+2x)}$. The structural fingerprint of each material was established by calculating the amplitude ratio $[P_xO_y]/[All]$ for each of the four peaks, where $[P_xO_y]$ is the amplitude of the specific vibrational mode at a fixed value of Raman shift, and [All] the total amplitude of the four vibrational modes considered. It should be noted that this amplitude ratio provides qualitative information only, as peak broadening or interferences for example may affect the results.

Evolution of these four ratios as a function of the lithium content in the sample is shown in **Figure 11**. This qualitative result shows a consistent and continuous evolution of the populations of more or less condensed structural units. Note that when the ratio value falls below 0.1, it can be considered as zero, insofar as this value may result from other nearby effects. It can be seen that the contribution of PO_3^- species is maximal for the lowest lithium contents, and minimal or nil for the highest lithium contents, while the opposite trend is observed for PO_4^{3-} entities. As for the $P_2O_7^4$ units, it appears that they are present in all samples in a relatively stable amount, as also shown in Figure 10b. Finally, it appears that the evolution of the contribution at 1110 cm^{-1} as a function of the Li content is very similar to that of PO_3^-. Therefore, it can be considered that the vibration observed corresponds to highly condensed entities. Additionally, due to its persistence at intermediate lithium levels, it is unlikely that the vibration corresponds to entities bound to a tri-coordinated nitrogen. Finally, the most likely attribution would be the contribution of entities sharing a di-coordinated N in segments of $PO_{3-2x}N_x^{-(1-x)}$ linear chains.

4. Use of Principal Component Analysis (PCA) to Get an Overview of the Material Library

This simple method of processing Raman spectra makes it possible to track the evolution of the structure by monitoring these different ratios, but it ignores the other information contained in the spectra. The use of PCA, on the other hand, allows for a more comprehensive treatment of all spectra. This was carried out using the dedicated module of the Origin software with a covariance matrix. This analysis shows that the information contained in the spectra can be summarized in two Principal Components (PC), which account for a total of 97.5% of the variance. The PCs were PC1 accounting for 88.18% and PC2 for 9.32%, and their loading plots are displayed in **Figure 12**a,b in order to visualize the PC distribution in the sample library. At first, we can clearly see that both PCs take into account main peaks selected previously; 953 cm^{-1} ↔ PO_4^{3-}; 1025 cm^{-1} ↔ $P_2O_7^{4-}$; 1167 cm^{-1} ↔ hypothetical $PO_{3-2x}N_x^{-(1-x)}$ Finally, three vibrational modes are highlighted between 650 and 840 cm^{-1}, but it is still unclear whether they

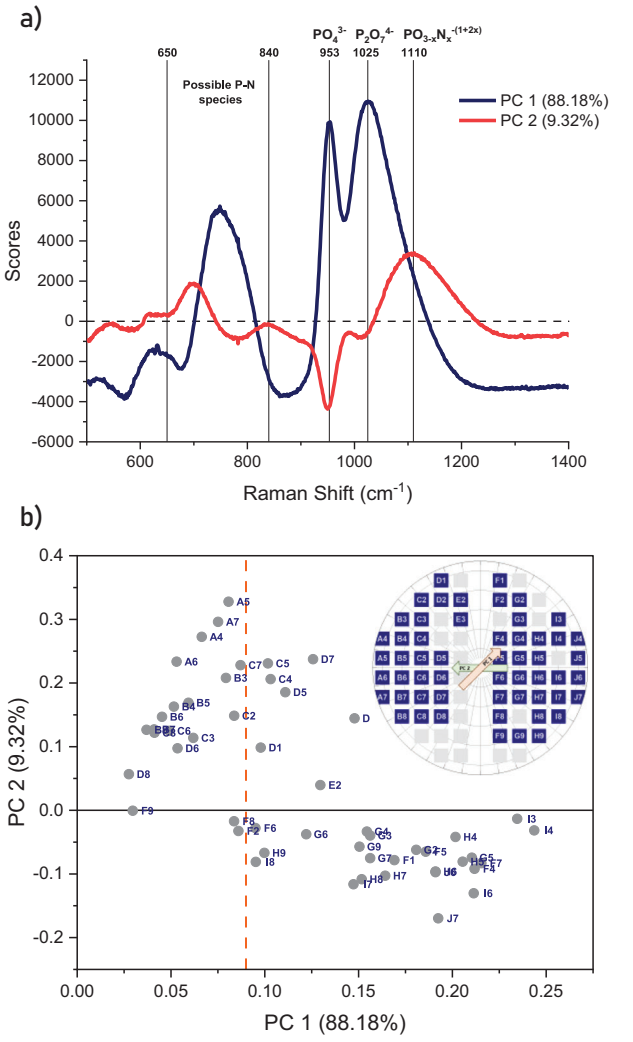

Figure 12. PCA analysis of the Raman dataset: a) score plot and b) loading plot (inset: location of the microcells included in the dataset).

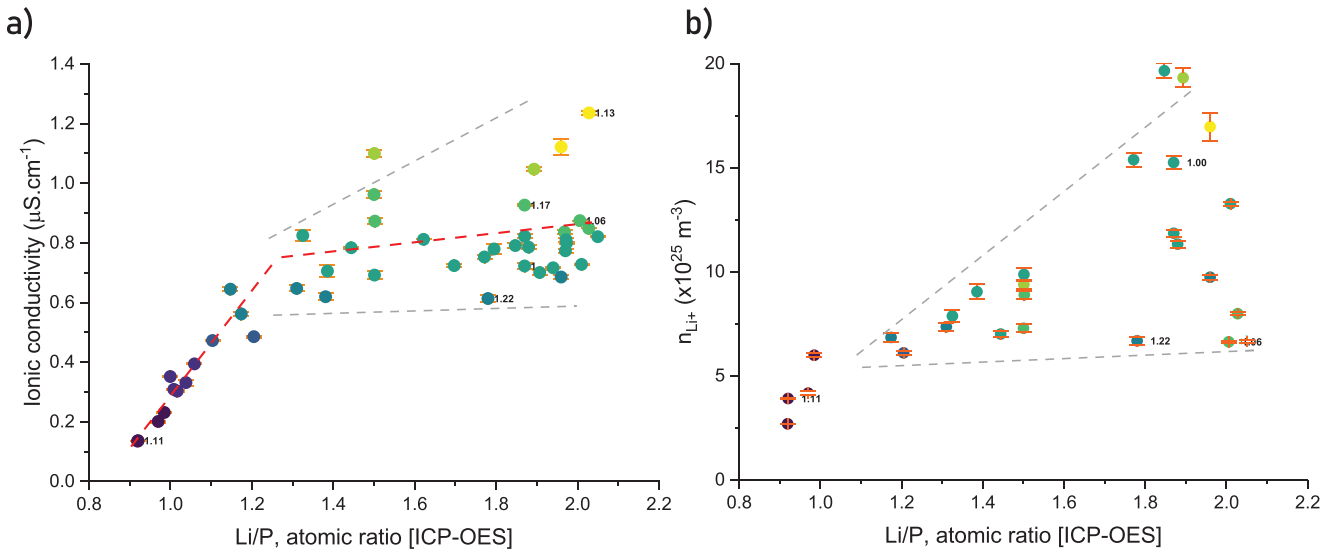

Figure 13. a) Ionic conductivity, and b) charge carrier density of the $Li_xPO_yN_z$ samples as a function of x. Additional labels stand for the z value, as obtained by RBS.

are attributable to PO_3^- (Figure 10b), or to oxynitride entities, as suggested by the literature.

Besides, the loading plot presented in Figure 12b displays the position of the microcells in PC1, PC2 coordinates. The whole dataset is distributed between [0.03; 0.25] for PC1 and [−0.20; 0.35] for PC2. Therefore, the former composes all Raman spectra. Meanwhile, PC2 presents an intricate behavior. Negative eigenvalues mean anticorrelated behavior, which is the case for 953 cm^{-1} and 1110 cm^{-1} peaks. While PC1 shows a predominance of 953 cm^{-1} (PO_4^{3-}) and of 1025 cm^{-1} ($P_2O_7^{4-}$) in all microcells, PC2 bears the consequence of *BB* condensation with i) positive values meaning a 1110 cm^{-1} contribution (hypothetical $PO_{3-x}N_x^{-(1+2x)}$ condensed *BB*) or ii) negative values meaning a 953 cm^{-1} and a slight 1025 cm^{-1} contribution.

Moreover, a distribution seems to appear from microcells label *"A"* with main contributions of positive PC2, up to microcells labelled *"I"* or *"J"*, and negative eigenvalues of PC2.

PCA applied to this series of Raman spectra displays loadings that are clearly interpretable. Actually, PC1 is related to the Raman peaks of PO_4^{3-} at 953 cm^{-1} and $P_2O_7^{4-}$ at 1025 cm^{-1}. In practice, it means that the microcells *D8* and *F9* present the least signal corresponding to these peaks and thus the less amount of these species. Conversely, microcells I3 and I4 present the highest peaks and so the highest amounts of these species in all the dataset. Similarly, PC2 is positively correlated to the Raman peak at 1100 cm^{-1} and negatively correlated to the Raman peak at 953 cm^{-1}. Thus, considering the dashed vertical line displayed in Figure 12b, it means that the intensity of the peak at 1100cm^{-1} is the highest and the one at 543 cm^{-1} the lowest for the *A5* microcell, while it is the contrary for the I8 microcell. Those observations confirmed the first hint given thanks to amplitude ratios (section III.d.i).

In conclusion, PC1 appears to correspond approximately to an axis oriented at 45° on the microcell library (see insert in Figure 12b), while PC2 appears to correspond approximately to the horizontal axis. This result is consistent with the gradients of parameters already evidenced within the microcell library.

4.1. Overview of Composition-Structure-Functional Properties

Throughout the characterization workflow, most key properties within the composition-structure-functional properties relationship have been unveiled for the material library. Therefore, a thorough study aims to understand beyond the mechanisms of this $Li_xPO_yN_z$ library. Thus, composition-structure-ionic conductivity are investigated using the entire dataset.

4.1.1. Correlating Functional Properties and Composition

At first, let us simply consider the evolution of conduction properties as a function of chemical composition alone. **Figure 13** presents a) ionic conductivity, and b) charge carrier density along Li/P ratio.

A linear increase in conductivity from 0.1 to ≈ 0.8 µS.cm^{-1} with increasing Li/P is observed in the interval [0.9; 1.3]. Above Li/P = 1.3, a trend towards stabilization of the conductivity value is then observed, accompanied by an increase in the distribution of the data. One hypothesis to explain this behavior for materials with 1.3<Li/P<2.1, is that nitrogen may facilitate the Li^+ migration within the material. Indeed, it is well known for the $Li_xPO_yN_z$ that nitrogen incorporation, at a fixed Li/P ratio, mitigates the enthalpy of migration,[49] and is therefore beneficial to the ionic conductivity.[49,56,57,65] Moreover, RBS analysis on some of this $Li_xPO_yN_z$ library have shown the dissimilarity of N content at close Li/P ratio, i.e., H2 = 1.13 N/P, J4 = 1.06 N/P with a close Li/P = 2.02 ± 0.01.

Upon examination of the evolution of charge carrier concentration as a function of the Li/P ratio alone, it is evident that the wide distribution of the dataset precludes the existence of a

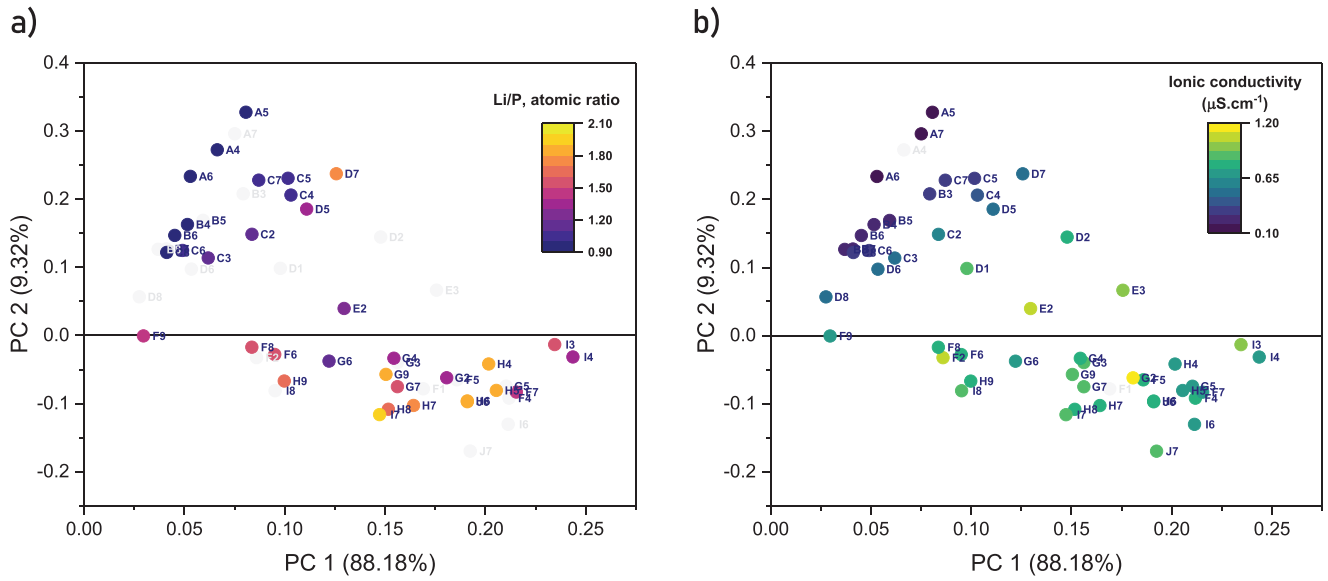

Figure 14. Cross-referencing of composition, conduction and structure data by representation of the a) Li/P ratio and b) ionic conductivity in the PC1-PC2 plane.

clear correlation between the two. At best, an overall trend for the charge carrier concentration to increase with increasing Li/P ratio can be inferred, which would seem quite logical. The influence of various nitrogen contents for a similar Li/P ratio in the samples could have possibly explained the variability observed. Nevertheless, *Landry* et al. have shown that the N content in materials having Li/P ≈ 3 does not influence the enthalpy of defect formation associated to Li^+, and hence the charge carrier concentration at high Li/P.[49] Furthermore, the N/P contents of four of our samples that were determined by RBS and are displayed on Figure 13b, do not highlight a specific trend in this respect. Within our specific composition range of [0.9; 2.1], the effect of nitrogen does not allow to conclude on this point. Thus, it will not be detailed further.

4.1.2. Functional Properties and Composition in the Framework of Structural Evolution

To elucidate further, a more comprehensive understanding of composition-structure-ionic conductivity relationships can be achieved by coupling the Raman dataset. As it was noticed previously, the PCA analysis takes into account most of the information. Moreover, the coupling of loading plot and score plot gives an interesting overview of the evolution of the structural units within the material library. The identical PCA plots are displayed (**Figure 14**) with slight changes. Variables are added as a color for all microcell vectors: a) showing Li/P atomic ratio, and b) ionic conductivity variations.

As noticed previously, a distribution of microcells is observed from the ones labelled *A* up to *J*. This shows the continuous distribution of structural units within the material library, i.e., from condensed oxy(nitride) phosphates network such as $PO_{3-x}N_x^{-(1+2x)}$ (hypothetical), PO_3^- to phosphate units like PO_4^{3-}, $P_2O_7^{4-}$. This list of structural units is not exhaustive. Other species have been identified in the literature, but have not been detected here by Raman spectroscopy.

Then, Li/P atomic ratio and ionic conductivity values have been plotted using the PCA dataset (Figure 14a,b). An evolution of the Li/P ratio going from 0.92 to 2.05 is observed along the distribution of the structural units. Thus, an increase in the Li/P atomic ratio explains the disappearance of condensed structural units and the emergence of uncondensed ones. Moreover, as expected from Figure 13a, the ionic conductivity of the material is closely linked to the composition, thus the structure. Figure 14b shows the σ_{Li+} distribution associated with the PCA dataset. A clear gradient is observed, which follows two trends: the substitution of condensed units for uncondensed ones (indicated by the label distribution), and the Li/P atomic ratio distribution. This is in agreement with the trend in ionic conductivity, which varies with the Li/P atomic ratio (Figure 13a) and with the expected structural units identified in the literature for given compositions, i.e., Li-rich or Li-poor $Li_xPO_yN_z$.

Thus, Figure 14 illustrates PCA's capability to highlight the intertwined relationships between composition, structure, and functional properties, as well as its capacity to process and represent a large dataset produced by multiple characterizations.

5. Conclusion

A high-throughput screening method has been developed for the study of solid Li^+ ionic conductors. This method allowed the simultaneous preparation of dozens of samples of different compositions by magnetron co-sputtering, and the rapid determination of their electrical properties. By using quantitative analysis techniques such as ICP-OES, RBS and NRA for calibration, we were able to demonstrate that true high-throughput quantitative analysis could be performed on these Li-containing thin film samples using LIBS. In terms of structural analysis, Raman

spectroscopy in automated mode proved to be perfectly suited to the chosen case study.

This methodology, applied to a case study, allowed us to study for the first time a large number of samples in the LiPON amorphous conductor system that were prepared as a homogeneous batch in terms of processing conditions and characterized together by the various techniques mentioned. The library of LiPON materials obtained under the chosen synthesis conditions represents a wide compositional range of $0.95 < Li/P < 2.03$, with a high N/P nitrogen content of about 1.0-1.2. The compositional range thus extends into an intermediate zone between the domain of bulk oxynitride glasses and that of traditional thin film LiPONs.

A number of correlations can be made by studying the joint evolution of functional properties, chemical composition and structural features on such a large group of samples. In particular, the ionic conductivity increases with Li content and begins to stabilize at around 10^{-6} S.cm^{-1} for Li/P >1.2. As the concentration of mobile carriers continues to increase with Li/P ratio, we observe that a gradual decrease in carrier mobility begins at this level, probably reflecting a change in the charge transport mechanism. In term of structure, this transition more or less coincides with the disappearance of PO_3^- chains in the materials. For the moment, this synthesis alone has not made it possible to study the influence of the nitrogen content, since the latter was relatively constant throughout the library. This can be expected because nitrogen is not a constituent of the targets and its incorporation is governed by other process parameters. Besides, we were able to confirm the attribution of certain Raman signals and to identify a specific contribution of condensed oxynitride by following the gradual evolution of the spectra across a wide range of Li/P compositions.

This work has made it possible to lay down the foundations for a new methodology for the study of solid electrolytes, some aspects of which still need to be refined, but which should prove powerful in understanding the cross-influences between composition-structure-functional properties. New developments in LIBS analysis, enabling high throughput quantitative analysis of elements such as H, O, N and S could make a major contribution to the success of the method as a whole.

Supporting Information

Supporting Information is available from the Wiley Online Library or from the author.

Acknowledgements

This project has received funding from the European Union's Horizon 2020 research and innovation programme under grant agreement No 957189. The project is part of BATTERY 2030+, the large-scale European research initiative for inventing the sustainable batteries of the future. The authors thank the AIFIRA facility, financially supported by the CNRS, the University of Bordeaux and the Région Nouvelle Aquitaine. We thank the technical staff members of the AIFIRA facility P. Alfaurt, J. Jouve and S. Sorieul. In addition, we thank Région Nouvelle Aquitaine (France) for their financial support.

Conflict of Interest

The authors declare no conflict of interest.

Data Availability Statement

The data that support the findings of this study are available from the corresponding author upon reasonable request.

Keywords

combinatorial synthesis, high throughput screening, laser-induced breakdown spectroscopy, lithium phosphorus oxynitride (LiPON), solid electrolytes

Received: February 7, 2024
Revised: May 28, 2024
Published online:

[1] M. Tatsumisago, T. Minami, *Mater. Chem. Phys.* **1987**, *18*, 1.
[2] A. R. Kulkarni, H. S. Maiti, A. Paul, *Bull. Mater. Sci.* **1984**, *6*, 201.
[3] A. Levasseur, J.-C. Brethous, J.-M. Réau, P. Hagenmuller, *Mater. Res. Bull.* **1979**, *14*, 921.
[4] A. Levasseur, M. Kbala, P. Hagenmuller, G. Couturier, Y. Danto, *Solid State Ionics* **1983**, *9–10*, 1439.
[5] Y. Yoon, C. Park, J. Kim, D. Shin, *Electrochim. Acta* **2013**, *111*, 144.
[6] B. Fleutot, B. Pecquenard, F. Le Cras, B. Delis, H. Martinez, L. Dupont, D. Guy-Bouyssou, *J. Power Sources* **2011**, *196*, 10289.
[7] A. S. Westover, M. Kornbluth, T. Egami, J. Liu, S. Kalnaus, D. Ma, A. K. Kercher, J. C. Neuefeind, M. Everett, V. Torres, S. W. Martin, B. Kozinsky, N. J. Dudney, *Chem. Mater.* **2023**, *35*, 2730.
[8] N. J. Dudney, J. B. Bates, J. D. Robertson, *J. Vac. Sci. Technol. A* **1993**, *11*, 377.
[9] S. Furusawa, T. Kasahara, A. Kamiyama, *Solid State Ionics* **2009**, *180*, 649.
[10] Y. Yoneda, C. Hotehama, A. Sakuda, M. Tatsumisago, A. Hayashi, *J. Ceram. Soc. Jpn* **2021**, *129*, 458.
[11] T. Kimura, A. Inoue, K. Nagao, T. Inaoka, H. Kowada, A. Sakuda, M. Tatsumisago, A. Hayashi, *ACS Appl. Energy Mater.* **2022**, *5*, 1421.
[12] B. Wang, B. S. Kwak, B. C. Sales, J. B. Bates, *J. Non-Cryst. Solids* **1995**, *183*, 297.
[13] J. B. Bates, N. J. Dudney, G. R. Gruzalski, R. A. Zuhr, A. Choudhury, C. F. Luck, J. D. Robertson, *Solid State Ionics* **1992**, *53–56*, 647.
[14] F. Michel, F. Kuhl, M. Becker, J. Janek, A. Polity, *Phys. Status Solidi B* **2019**, *256*, 1900047.
[15] S. W. Martin, C. A. Angell, *J. Non-Cryst. Solids* **1986**, *83*, 185.
[16] R. Marchand, *J. Non-Cryst. Solids* **1983**, *56*, 173.
[17] R. W. Larson, D. E. Day, *J. Non-Cryst. Solids* **1986**, *88*, 97.
[18] N. Mascaraque, J. L. G. Fierro, A. Durán, F. Muñoz, *Solid State Ionics* **2013**, *233*, 73.
[19] N. Mascaraque, H. Takebe, G. Tricot, J. L. G. Fierro, A. Durán, F. Muñoz, *J. Non-Cryst. Solids* **2014**, *405*, 159.
[20] A. Magistris, G. Chiodelli, M. Villa, *J. Power Sources* **1985**, *14*, 87.
[21] P. P. Tsai, M. Greenblatt, *J. Non-Cryst. Solids* **1988**, *103*, 101.
[22] B. Wang, B. C. Chakoumakos, B. C. Sales, B. S. Kwak, J. B. Bates, *J. Solid State Chem.* **1995**, *115*, 313.
[23] N. Suzuki, T. Inaba, T. Shiga, *Thin Solid Films* **2012**, *520*, 1821.
[24] Y. Hamon, A. Douard, F. Sabary, C. Marcel, P. Vinatier, B. Pecquenard, A. Levasseur, *Solid State Ionics* **2006**, *177*, 257.
[25] C. Park, S. Lee, S. Choi, D. Shin, *Thin Solid Films* **2019**, *685*, 434.
[26] T. Famprikis, J. Galipaud, O. Clemens, B. Pecquenard, F. Le Cras, *ACS Appl. Energy Mater.* **2019**, *2*, 4782.
[27] C. R. Brown, E. McCalla, C. Watson, J. R. Dahn, *ACS Comb. Sci.* **2015**, *17*, 381.
[28] S. D. Beattie, J. R. Dahn, *J. Electrochem. Soc.* **2005**, *152*, C542.

[29] B. Khanetskyy, D. Dallinger, C. O. Kappe, *J. Comb. Chem.* **2004**, *6*, 884.
[30] S. S. Mao, *J. Cryst. Growth* **2013**, *379*, 123.
[31] T. D. Hatchard, J. M. Topple, M. D. Fleischauer, J. R. Dahn, *Electrochem. Solid-State Lett.* **2003**, *6*, A129.
[32] J. S. Cooper, G. Zhang, P. J. McGinn, *Rev. Sci. Instr.* **2005**, *76*, 062221.
[33] Y. Liu, J. Padmanabhan, B. Cheung, J. Liu, Z. Chen, B. E. Scanley, D. Wesolowski, M. Pressley, C. C. Broadbridge, S. Altman, U. D. Schwarz, T. R. Kyriakides, J. Schroers, *Sci. Rep.* **2016**, *6*, 26950.
[34] F. L.e Cras, B. Pecquenard, V. Dubois, V.-P. Phan, D. Guy-Bouyssou, *Adv. Energy Mater.* **2015**, *5*, 1501061.
[35] H.-K. Kim, T.-Y. Seong, J.-H. Lim, W. Ii Cho, Y. Soo Yoon, *J. Power Sources* **2001**, *102*, 167.
[36] K. Ahuja, V. Sallaz, R. B. Nuwayhid, F. Voiron, P. McCluskey, G. W. Rubloff, K. E. Gregorczyk, *J. Power Sources* **2023**, *575*, 233056.
[37] J. B. Bates, N. J. Dudney, G. R. Gruzalski, R. A. Zuhr, A. Choudhury, C. F. Luck, J. D. Robertson, *J. Power Sources* **1993**, *43*, 103.
[38] A. Schwöbel, R. Hausbrand, W. Jaegermann, *Solid State Ionics* **2015**, *273*, 51.
[39] W. C. West, J. F. Whitacre, J. R. Lim, *J. Power Sources* **2004**, *126*, 134.
[40] S. Borhani-Haghighi, M. Kieschnick, Y. Motemani, A. Savan, D. Rogalla, H.-W. Becker, J. Meijer, A. Ludwig, *ACS Comb. Sci.* **2013**, *15*, 401.
[41] F. J. Fortes, J. Moros, P. Lucena, L. M. Cabalín, J. J. Laserna, *Anal. Chem.* **2013**, *85*, 640.
[42] W. Berthou, M. Legallais, B. Bousquet, V. Motto-Ros, F. Le Cras, *Spectrochim. Acta B: At. Spectrosc.* **2024**, *215*, 106906.
[43] L. Han, C.-T. Hsieh, B. C. Mallick, J. Li, Y. A. Gandomi, *Nanoscale Adv.* **2021**, *3*, 2728.
[44] M. Nisula, Y. Shindo, H. Koga, M. Karppinen, *Chem. Mater.* **2015**, *27*, 6987.
[45] V. Chevrier, J. R. Dahn, *Meas. Sci. Technol.* **2006**, *17*, 1399.
[46] V. Motto-Ros, S. Moncayo, F. Trichard, F. Pelascini, *Spectrochim. Acta B: At. Spectrosc.* **2019**, *155*, 127.
[47] L. Le Van-Jodin, F. Ducroquet, F. Sabary, I. Chevalier, *Solid State Ionics* **2013**, *253*, 151.
[48] P. Barberet, J. Jouve, S. Sorieul, P. Alfaurt, L. Mathieu, *Eur Phys J Plus* **2021**, *136*, 67.
[49] A.-K. Landry, R. Bayzou, A. Benayad, J. Trébosc, F. Pourpoint, O. Lafon, F. Le Cras, B. Pecquenard-Le Cras, R. B. Nuernberg, *Chem. Mater.* **2023**, *35*, 9313.
[50] H. Kahnt, *J. Non-Cryst. Solids* **1996**, *203*, 225.
[51] Z.-W. Fu, W.-Y. Liu, C.-L. Li, Q.-Z. Qin, Y. Yao, F. Lu, *App. Phys. Lett.* **2003**, *83*, 5008.
[52] F. Poggialini, B. Campanella, B. Cocciaro, G. Lorenzetti, V. Palleschi, S. Legnaioli, *J. Anal. At. Spectrom.* **2023**, *38*, 1751.
[53] J. Hermann, E. Axente, F. Pelascini, V. Craciun, *Anal. Chem.* **2019**, *91*, 2544.
[54] C. Jeynes, J. L. Colaux, *Analyst* **2016**, *141*, 5944.
[55] R. Marchand, D. Agliz, L. Boukbir, A. Quemerais, *J. Non-Cryst. Solids* **1988**, *103*, 35.
[56] R. Bayzou, J. Trébosc, A.-K. Landry, R. B. Nuernberg, B. Pecquenard-Le Cras, F. Le Cras, F. Pourpoint, O. Lafon, *J. Magn. Reson.* **2023**, *354*, 107530.
[57] V. Lacivita, N. Artrith, G. Ceder, *Chem. Mater.* **2018**, *30*, 7077.
[58] S. V. Pershina, A. A. Raskovalov, B. D. Antonov, O. G. Reznitskikh, E. G. Vovkotrub, N. N. Batalov, N. I. Kadyrova, *Russ. J. Phys. Chem.* **2016**, *90*, 2194.
[59] B. V. R. Chowdari, K. L. Tan, W. T. Chia, *Solid State Ionics* **1992**, *53*, 1172.
[60] L. Le Van-Jodin, A. Claudel, C. Secouard, F. Sabary, J.-P. Barnes, S. Martin, *Electrochim. Acta* **2018**, *259*, 742.
[61] T. Pichonat, C. Lethien, N. Tiercelin, S. Godey, E. Pichonat, P. Roussel, M. Colmont, P. A. Rolland, *Mater. Chem. Phys.* **2010**, *123*, 231.
[62] B. Fleutot, B. Pecquenard, H. Martinez, M. Letellier, A. Levasseur, *Solid State Ionics* **2011**, *186*, 29.
[63] M. A. Carrillo Solano, M. Dussauze, P. Vinatier, L. Croguennec, E. I. Kamitsos, R. Hausbrand, W. Jaegermann, *Ionics* **2016**, *22*, 471.
[64] B. Yari, P. Sauriol, J. Chaouki, *Can. J. Chem. Eng.* **2019**, *97*, 2273.
[65] V. Lacivita, A. Westover, A. Kercher, N. Phillip, G. Yang, G. Veith, G. Ceder, N. Dudney, *J. Am. Chem. Soc.* **2018**, *140*, 11029.